

# Scaled boundary polygon formula for Cosserat continuum and its verification

Kai Chen<sup>a,b</sup>, Degao Zou<sup>a,b</sup>, Hongxiang Tang<sup>a,c,\*</sup>, Jingmao Liu<sup>a,b</sup>, Yue Zhuo<sup>a,b</sup>

<sup>a</sup> The State Key Laboratory of Coastal and Offshore Engineering, Dalian University of Technology, Dalian, Liaoning 116024, China

<sup>b</sup> School of Hydraulic Engineering, Dalian University of Technology, Dalian, Liaoning 116024, China

<sup>c</sup> School of Civil Engineering, Dalian University of Technology, Dalian, Liaoning 116024, China

## ARTICLE INFO

### Keywords:

Scaled Boundary FEM  
Polygonal Cosserat continuum method  
Stress concentration  
Incompressible material  
Opening structures

## ABSTRACT

Cosserat continuum method can be used to solve stress concentration of holes. However, with the shape limitation of its elements, it is worthwhile to improve the element quality so that this method can be universal and feasible to complex situations. In this paper, a flexible polygonal Cosserat continuum analysis method is firstly deduced and numerically developed based on the theory of Scaled Boundary FEM. Stress concentration on the holes embedded in different structures is then investigated using the proposed method and verified against the theoretical solution, which not only shows good agreement, but also reasonably weakens the stress concentration. The proposed method can closely replicate the theoretical solution for the case when the material is nearly incompressible (Poisson's ratio close to 0.5), also indicating the robustness of this method. Additionally, complex polygonal elements can be solved directly, coupling the quadtree and polygon discretization techniques seamlessly, wherein the efficiency and convenience are improved for processing complex geometries. The proposed method can provide important technical support for stress concentration analysis of structures with complex holes, and contribute to facilitating shape optimization of holes design.

## 1. Introduction

For the consideration of aesthetics, functional requirements, and material optimization, holes play an important role in many fields of structural design (e.g. in civil and hydraulic engineering, mechanical engineering, aerospace engineering, medical bioengineering, etc.). Besides, a considerable micropores have also been observed in some structures, because of material defects (such as 3D printing structure [1]).

However, local high stress would emerge inevitably, when the structure shape changes rapidly (e.g. orifice). This phenomenon is called stress concentration, as a consequence, the fatigue cracks could be induced unavoidably in the long-term operation service, subsequently, leading to fractures or damages, and eventually, shorten the service life of the structure, and may even induce serious secondary damage. As a result, it is of great significance to simulate the stress concentration of the opening reasonably and effectively so that the stress state of the structure can be revealed accurately.

Based on the classical theory of elasticity, abundant researches have been carried out worldwide on stress concentration at the hole edge. Some key works are listed as follows: the plane complex function [2] is

proposed to solve the stress concentration problem effectively, containing a single hole. Kirsch presented a real function method [3], which can be used to obtain the stress distribution easily. The series expansion method and the corresponding improved method [4–7] can deal with the multihole problems under certain conditions. Schwarz alternating method [8,9] provides an effective way to solve the plane multihole problems, in which the selection of iterative technique is very important. With the development of finite element theory and boundary element technology [10–12], in terms of macro mechanical response, the problems involved with nonlinearity and anisotropy have been alleviated effectively, making the analytical scale significantly improved.

The mechanical properties of materials (including the stress concentration at the orifice) is closely related to the microstructure of materials, which is difficult to be considered in the numerical method based on classical continuum theory. In Cosserat continuum, the rotational degrees of freedom, the micro-curvatures as spatial derivatives of the rotational degrees of freedom, the coupled stresses energetically conjugate to the micro-curvatures and the material parameter called internal length scale, which is interrelated to material microstructure, are introduced. In doing so, the shear band failure induced by localized strain can

\* Corresponding author.

E-mail addresses: [chenkai@dlut.edu.cn](mailto:chenkai@dlut.edu.cn) (K. Chen), [tanghx@dlut.edu.cn](mailto:tanghx@dlut.edu.cn) (H. Tang).

be simulated effectually [13–17]. Moreover, combining with the finite element theory, the stress concentration of the orifice and the structural microeffect can be investigated with satisfactory. Thus, the practicability of the Cosserat continuum method [18–20] is further enhanced. In the development of Cosserat methodology, Providas et al. [21] derived and numerically developed three kinds of plane triangle Cosserat elements; Zhang et al. presented a quadrilateral isoparametric element analysis method [22]; Tang et al. developed a Cosserat low-order mixed element [23]. Furthermore, Khoei et al. [24] put forward the Cosserat continuum method for solving three-dimensional space problems; Godio et al. [25] extended the application to a dynamic analysis of plates; A Cosserat continuum numerical method is achieved in the works of Alsaleh et al. [26] and Tang et al. [27], aiming to investigate the shear band observed in coarse-grained soil. Overall speaking, the Cosserat theory has developed rapidly and has been widely adopted, which would have a good application prospect.

With the development of computer technology, abundant new ideas and concepts have been introduced into structural design. More complex structures are designed involving various forms of opening and maldistribution in space. The frequently-used method based on isoparametric theory has limitations on meshing shapes (quadrilateral, hexahedral, and degenerate conditions), therefore may require frequent manual interactions, and lead to low-grade automation when processing complex geometric boundaries. Consequently, the pre-processing process is cumbersome and inefficient when the Cosserat FEM is applied to the analysis of complex structures. The application performance and development potential can be improved once the universality and flexibility of Cosserat FEM can be optimized.

Polygons possess comparable generality and flexibility relative to quadrilateral elements, which can enhance the adaptability to complex boundary, therefore more matured developments and applications [28–31] can be achieved. Among them, the Scaled Boundary Finite Element Method (SBFEM) [32] is an emerging numerical methodology, equipped with the advantages of dimension reduction, easy-construct polygon and simple data structure. It has made significant progress and been used in applications in electromagnetics [33], crack propagation [34–40] (momentous and novel alternative approaches to failure analysis), transient wave propagation [41], soil-structure interaction [42], thermology [43], fluid-solid coupling [44,45], complex element technique [46,47], geotechnical nonlinear analysis [48–50], analysis of sandwich plates [51–53], damage simulation of structures [54–58] and other fields, solving many practical problems in researches.

Recently, on the strength of the development of automatic image-based discretization technology [32,46,59], the analysis performance of SBFEM is further enhanced. Inspired by these works, a combination of the SBFEM with the spectral cell method (SCM) is proposed, to overcome suboptimal convergence due to the inaccurate representation of the boundary [60], and transient analyses of complex geometries are studied. Subsequently, the image-based approach has been extended to the thermal conductivity of heterogeneous materials [61] and the elastoplastic simulation of complex structures [62]. Overall, it can be considered that SBFEM combined with image-based discretization method can effectively manage many problems in automatic simulation of complex structures, and has a good guiding role for the follow-up researches and applications in related fields.

In this paper, a newly analysis method of plane Cosserat polygon element is derived and numerically developed, based on the framework of SBFEM theory. Then, this method is verified against theoretical solution on an example simulation of a circular hole on an infinite thin plate, and further stability is strengthened when simulating a nearly incompressible material of the same case. On the whole, a higher accuracy has been observed using the proposed method, especially when the material is nearly incompressible. Subsequently, different opening hole forms are simulated, for the sake of examining the flexibility for complex geometries. Moreover, as the quadtree grids are introduced, the efficiency of complex structure analysis would be improved satisfactorily.

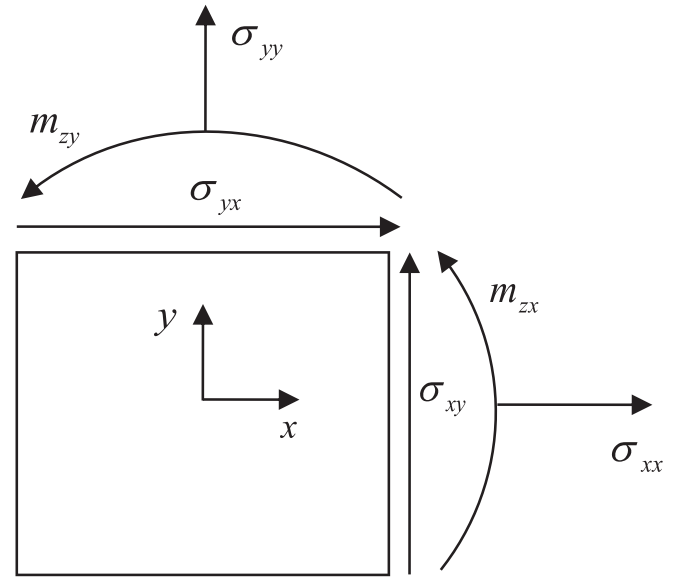


Fig. 1. stress and couple-stress in a two-dimensional Cosserat continuum.

## 2. SBFEM formulation for cosserat continuum

### 2.1. Synopsis of cosserat continuum

In the plane theory, each material point in the two dimensional Cosserat continuum has three degrees of freedom, and the displacement vector is expressed as follows:

$$\mathbf{u} = [u_x \ u_y \ \omega_z]^T \quad (1)$$

where  $u_x, u_y$  and  $\omega_z$  are translational and rotational DOFs, and the corresponding strain and stress vectors can be derived:

$$\boldsymbol{\varepsilon} = [\varepsilon_{xx} \ \varepsilon_{yy} \ \varepsilon_{zz} \ \varepsilon_{xy} \ \varepsilon_{yx} \ \kappa_{zx} l_c \ \kappa_{zy} l_c]^T \quad (2)$$

$$\boldsymbol{\sigma} = [\sigma_{xx} \ \sigma_{yy} \ \sigma_{zz} \ \sigma_{xy} \ \sigma_{yx} \ m_{zx}/l_c \ m_{zy}/l_c]^T \quad (3)$$

In Eqs. (2) and (3),  $\kappa_{zx}, \kappa_{zy}$  represent micro curvatures,  $m_{zx}, m_{zy}$  are the corresponding couple stresses (as shown in Fig. 1),  $l_c$  indicates the internal length parameter of the material.

In the theory of elasticity, the strain displacement relationship and the mechanical equilibrium equation can be expressed as

$$\boldsymbol{\varepsilon} = \mathbf{L} \mathbf{u} \quad (4)$$

$$\mathbf{L}^T \boldsymbol{\sigma} + \mathbf{f} = \mathbf{0} \quad (5)$$

where the linear operator matrix  $\mathbf{L}$  is written as

$$\mathbf{L}^T = \begin{bmatrix} \frac{\partial}{\partial x} & 0 & 0 & 0 & \frac{\partial}{\partial y} & 0 & 0 \\ 0 & \frac{\partial}{\partial y} & 0 & \frac{\partial}{\partial x} & 0 & 0 & 0 \\ 0 & 0 & 0 & -1 & 1 & \frac{\partial}{\partial x} & \frac{\partial}{\partial y} \end{bmatrix} \quad (6)$$

The linear elastic stress-strain relationship is expressed as

$$\boldsymbol{\sigma} = \mathbf{D}_e \boldsymbol{\varepsilon}_e \quad (7)$$

with the isotropic modulus matrix  $\mathbf{D}_e$ , written as

$$\mathbf{D}_e = \begin{bmatrix} \lambda + 2G & \lambda & \lambda & 0 & 0 & 0 & 0 \\ \lambda & \lambda + 2G & \lambda & 0 & 0 & 0 & 0 \\ \lambda & \lambda & \lambda + 2G & 0 & 0 & 0 & 0 \\ 0 & 0 & 0 & G + G_c & G - G_c & 0 & 0 \\ 0 & 0 & 0 & G - G_c & G + G_c & 0 & 0 \\ 0 & 0 & 0 & 0 & 0 & 2G & 0 \\ 0 & 0 & 0 & 0 & 0 & 0 & 2G \end{bmatrix} \quad (8)$$

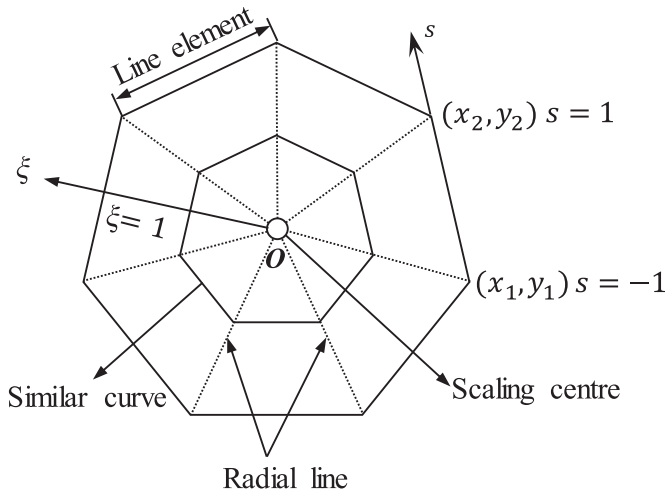


Fig. 2. Polygon representation of scaled boundary finite element method.

where  $\lambda = 2G\nu/(1 - \nu)$  is the Lamé constant,  $G$  and  $\nu$  are the shear modulus and Poisson's ratio in classical elasticity, and  $G_c$  is the Cosserat shear modulus.

## 2.2. Summary of scaled boundary finite element method

For any calculated domain,  $n$ -sided polygons can be used to perform the discretization ( $n$  is an arbitrary integer greater than 2) as long as each polygon meets the scale center requirements of SBFEM (the scale center can be directly seen from any point on the boundary). This can be regarded as an SBFEM sub-element. The numerical results of the whole problem can be obtained after each sub-element is solved separately.

This method is widely employed and abundant literature (e.g. [32]) can be referred. Therefore, only some key equations are introduced herein. A representative polygon element calculated using SBFEM is illustrated in Fig. 2, in which the scale center is defined in its geometric center. The boundary of a polygon is discretized via a one-dimensional line element, and the local coordinate system  $(\xi, s)$  is introduced, referring to the FEM. The radial coordinate  $\xi$  is taken as 0 at scale center  $O$  and becomes 1 at the boundary, as well as, the value of circular coordinates is set as  $-1 \leq s \leq 1$ . Then, the coordinates of any point on the line element can be obtained according to the node coordinates on the boundary, as shown in Eqs. (9) and (10).

$$\mathbf{x}_b(s) = \mathbf{N}(s)\mathbf{x}_b \quad (9)$$

$$\mathbf{y}_b(s) = \mathbf{N}(s)\mathbf{y}_b \quad (10)$$

$$\mathbf{N}(s) = [\mathbf{N}_1(s), \mathbf{N}_2(s), \mathbf{N}_3(s), \dots, \mathbf{N}_m(s)] \quad (11)$$

where  $\mathbf{N}(s)$  is the shape function of a line element contains  $m$  nodes, with unlimited order in Eq. (11). Only the boundaries are discretized for any elements, avoiding complex mesh generation for the degree raising of the shape function. As a result, the order of shape function can be increased according to the actual demands. The standard one-dimensional Gauss-Lobatto-Lagrange function is selected. After obtaining the geometric coordinates of the boundary, the coordinates of any point in the solved domain can be determined through the introduced radial coordinate  $\xi$ , as shown in Eqs. (12) and (13).

$$\mathbf{x}(\xi, s) = \xi \mathbf{N}(s)\mathbf{x}_b \quad (12)$$

$$\mathbf{y}(\xi, s) = \xi \mathbf{N}(s)\mathbf{y}_b \quad (13)$$

The displacement field of any point in the sector can be expressed in the form of Eq. (14) with SBFEM coordinates, which is formed by connecting the line between each boundary element and the scale center.

$$\mathbf{u}(\xi, s) = \mathbf{N}_u(s)\mathbf{u}(\xi) \quad (14)$$

where  $\mathbf{u}(\xi)$  is the radial displacement function, and  $\mathbf{N}_u(s)$  is the interpolation function of the boundary line element.

## 2.3. SBFEM formulation for Cosserat Continuum

In the framework of SBFEM, the formula of SBFEM-Cosserat is deduced and the polygon Cosserat element is constructed. As it is known, the following are relations between physical coordinates and parameter coordinates in isoparametric element:

$$\begin{bmatrix} \frac{\partial}{\partial \xi} \\ \frac{\partial}{\partial s} \end{bmatrix} = \mathbf{J} \begin{bmatrix} \frac{\partial}{\partial x} \\ \frac{\partial}{\partial y} \end{bmatrix}, \quad \mathbf{J} = \begin{bmatrix} 1 & \\ \xi & \end{bmatrix} \begin{bmatrix} x(s) & y(s) \\ x(s)_{,s} & y(s)_{,s} \end{bmatrix} \quad (15)$$

$$\begin{bmatrix} \frac{\partial}{\partial x} \\ \frac{\partial}{\partial y} \end{bmatrix} = \mathbf{J}^{-1} \begin{bmatrix} \frac{\partial}{\partial \xi} \\ \frac{\partial}{\partial s} \end{bmatrix} = \begin{bmatrix} y(s)_{,s} \frac{\partial}{\partial \xi} - \frac{1}{\xi} y(s) \frac{\partial}{\partial s} \\ -x(s)_{,s} \frac{\partial}{\partial \xi} + \frac{1}{\xi} x(s) \frac{\partial}{\partial s} \end{bmatrix} \quad (16)$$

By substituting the Eq. (6), the linear operator matrix  $\mathbf{L}$  for Cosserat continuum can be obtained:

$$\mathbf{L} = \mathbf{b}_1 \frac{\partial}{\partial \xi} + \frac{1}{\xi} \mathbf{b}_2 \frac{\partial}{\partial s} + \mathbf{b}_3 \quad (17)$$

where the formulations of coefficient matrix  $\mathbf{b}_i$  can be written as

$$\mathbf{b}_1^T = \begin{bmatrix} y(s)_{,s} & 0 & 0 & 0 & -x(s)_{,s} & 0 & 0 \\ 0 & -x(s)_{,s} & 0 & x(s)_{,s} & 0 & 0 & 0 \\ 0 & 0 & 0 & 0 & 0 & y(s)_{,s} & -x(s)_{,s} \end{bmatrix} \quad (18)$$

$$\mathbf{b}_2^T = \begin{bmatrix} -y(s) & 0 & 0 & 0 & x(s) & 0 & 0 \\ 0 & x(s) & 0 & -y(s) & 0 & 0 & 0 \\ 0 & 0 & 0 & 0 & 0 & -y(s) & x(s) \end{bmatrix} \quad (19)$$

$$\mathbf{b}_3^T = \begin{bmatrix} 0 & 0 & 0 & 0 & 0 & 0 & 0 \\ 0 & 0 & 0 & 0 & 0 & 0 & 0 \\ 0 & 0 & 0 & -1 & 1 & 0 & 0 \end{bmatrix} \quad (20)$$

By substituting Eq. (4) and Eq. (14), the expression of the strain matrix is expressed as

$$\boldsymbol{\epsilon} = \mathbf{B}_1^C \mathbf{u}(\xi)_{,\xi} + \frac{1}{\xi} \mathbf{B}_2^C \mathbf{u}(\xi) + \mathbf{B}_3^C \mathbf{u}(\xi) \quad (21)$$

$$\begin{aligned} \mathbf{B}_1^C(s) &= \mathbf{b}_1 \mathbf{N}_u(s) \\ \mathbf{B}_2^C(s) &= \mathbf{b}_2 \mathbf{N}_u(s)_{,s} \\ \mathbf{B}_3^C(s) &= \mathbf{b}_3 \mathbf{N}_u(s) \end{aligned} \quad (22)$$

In the formula, the radial displacement function  $\mathbf{u}(\xi)$  can be obtained by solving the SBFEM governing equation, as shown in the following:

$$\mathbf{E}_0 \xi^2 \mathbf{u}(\xi)_{,\xi\xi} + (\mathbf{E}_0 - \mathbf{E}_1 + \mathbf{E}_1^T) \xi \mathbf{u}(\xi)_{,\xi} - \mathbf{E}_2 \mathbf{u}(\xi) + \mathbf{F}(\xi) = 0 \quad (23)$$

Eq. (23) is a second-order non-homogeneous partial differential equation with  $\xi$  as a variable, where  $\mathbf{E}_i$  ( $i = 0, 1, 2$ ) is a coefficient matrix only related to material properties and geometry, and the expression is shown in Eq. (24).  $\mathbf{F}(\xi)$  is an external load vector. When  $\mathbf{F}(\xi)$  takes zero value, the equation can be transformed into a first-order homogeneous differential equation by introducing a variable  $\mathbf{X}(\xi)$ .

$$\mathbf{E}_0 = \int_{-1}^{+1} [\mathbf{B}_1^C]^T(s) \mathbf{D}_e [\mathbf{B}_1^C(s)] |\mathbf{J}(s)| ds \quad (24a)$$

$$\mathbf{E}_1 = \int_{-1}^{+1} [\mathbf{B}_2^C(s) + \mathbf{B}_3^C(s)]^T \mathbf{D}_e [\mathbf{B}_1^C(s)] |\mathbf{J}(s)| ds \quad (24b)$$

$$\mathbf{E}_2 = \int_{-1}^{+1} [\mathbf{B}_2^C(s) + \mathbf{B}_3^C(s)]^T \mathbf{D}_e [\mathbf{B}_2^C(s) + \mathbf{B}_3^C(s)] |\mathbf{J}(s)| ds \quad (24c)$$

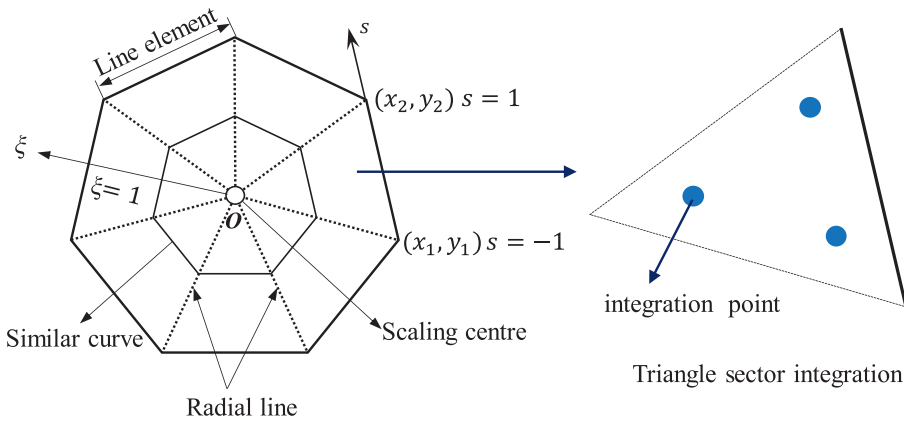


Fig. 3. Schematic diagram of integration on polygon element.

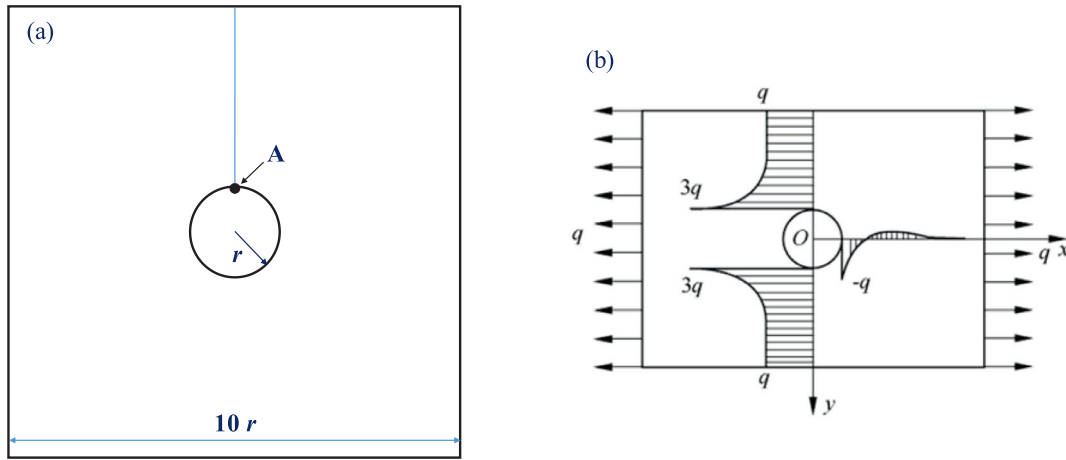


Fig. 4. Stress concentration problem of circular hole in rectangular plate: (a) geometric domain, and (b) classical continuous physical solution.

In the formula,  $D_e$  is the elastic constitutive matrix,  $|J(s)|$  represents Jacobian matrix determinant, and when the intermediate variable matrix  $X(\xi)$  is introduced, the Eq.(23) can be rewritten as

$$X(\xi) = \begin{Bmatrix} u(\xi) \\ q(\xi) \end{Bmatrix} \quad (25)$$

$$\xi X(\xi)_\xi = -ZX(\xi) \quad (26)$$

where the Hamilton matrix  $Z$  is expressed in Eq.(27), and  $q(\xi)$  is the corresponding internal node force vector of  $u(\xi)$ .

$$Z = \begin{bmatrix} E_0^{-1} E_1^T & -E_0^{-1} \\ E_1 E_0^{-1} E_1^T - E_2 & -E_1 E_0^{-1} \end{bmatrix} \quad (27)$$

After the eigenvalue decomposition is performed to the Hamilton matrix  $Z$ , the following equation can be obtained for each polygon element.

$$Z \begin{bmatrix} \psi_u \\ \psi_q \end{bmatrix} = \begin{bmatrix} \psi_u \\ \psi_q \end{bmatrix} S_n \quad (28)$$

where  $S_n$  is a diagonal matrix composed of negative eigenvalues generated from the decomposition of  $Z$  matrix,  $\psi_u$  and  $\psi_q$  are transformation matrices corresponding to displacement and stress modes, respectively. Then, for any polygon element, the solution of Eq. (23) is provided as follows:

$$\begin{aligned} u(\xi) &= \psi_u \xi^{-S_n} c_n \\ q(\xi) &= \psi_q \xi^{-S_n} c_n \end{aligned} \quad (29)$$

in which  $c_n$  is an integral constant matrix, and it can be solved from the node displacement  $u_b$  on the boundary of the polygon element. Thus, the

equivalent form function  $\Phi(\xi, s)$  can be obtained, similar to the FEM, and its expression is given as follows:

$$c_n = \psi_u^{-1} u_b \quad (30)$$

$$\Phi(\xi, s) = N_u(s) \psi_u \xi^{-S_n} \psi_u^{-1} \quad (31)$$

Substituting the displacement expression (29) into Eq. (21), the strain matrix can be rewritten as Eq. (32); then the strain-displacement matrix can be extracted.

$$\epsilon = ([B_1^C \psi_u [-S_n] + B_2^C \psi_u] \xi^{-S_n} \psi_u^{-1} + B_3^C \psi_u \xi^{-S_n} \psi_u^{-1}) u_b \quad (32)$$

$$B_u^C = [B_1^C \psi_u [-S_n] + B_2^C \psi_u] \xi^{-S_n} \psi_u^{-1} + B_3^C \psi_u \xi^{-S_n} \psi_u^{-1} \quad (33)$$

After calculating the node displacement, the displacement field in the element can be obtained via shape function interpolation. Similar to FEM, Eq. (34) can be obtained using the principle of virtual work.

$$\int_{\Omega} \delta \epsilon^T \Delta \sigma(\xi, s) d\Omega = \int_{\Gamma} \delta u^T f_t d\Gamma + \int_{\Gamma} \delta u^T f_b d\Gamma - \int_{\Omega} \delta \epsilon^T \sigma(\xi, s) d\Omega \quad (34)$$

where  $\Delta \sigma(\xi, s)$  represents stress increment,  $f_t$  and  $f_b$  are boundary shear force vector and bulk force density respectively, and  $\delta \epsilon(\xi, s)$  is virtual strain field corresponding to virtual displacement field  $\delta u(\xi, s)$ . Since the virtual strain can be taken as any value, a further deduction is conducted for each polygon element:

$$\begin{aligned} \left( \int_{\Omega} [B_u^C(\xi, s)]^T D_e [B_u^C(\xi, s)] d\Omega \right) \Delta u_b &= \left( \int_{\Gamma} \Phi^T(\xi, s) f_t d\Gamma + \int_{\Gamma} \Phi^T(\xi, s) f_b d\Omega \right) \\ &- \left( \int_{\Omega} [B_u^C(\xi, s)]^T \sigma(\xi, s) d\Omega \right) \end{aligned} \quad (35)$$

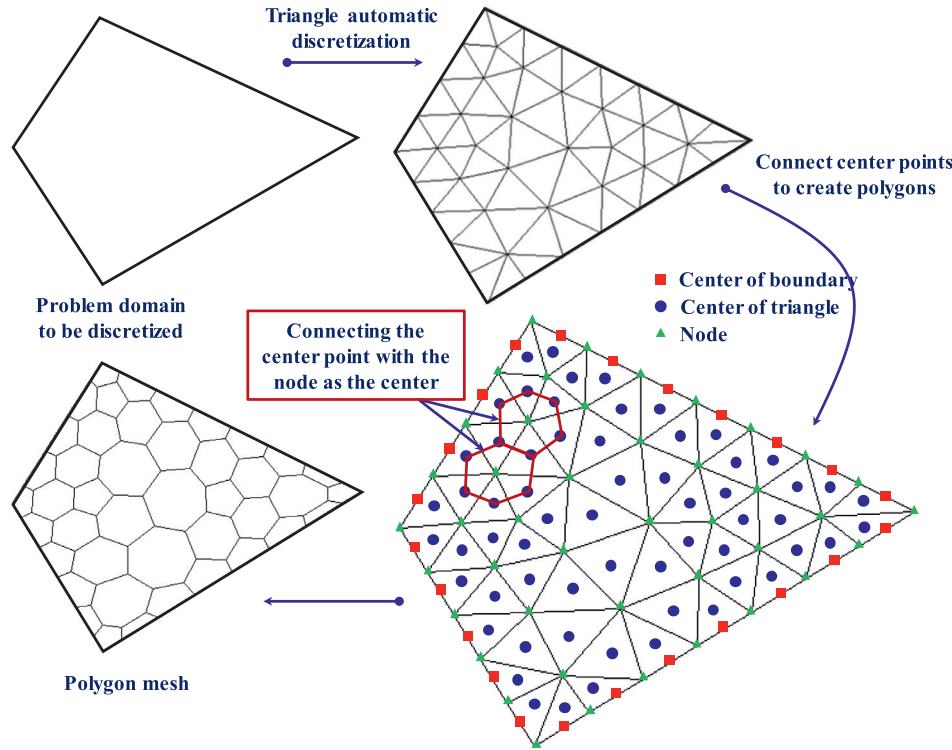


Fig. 5. Generation of polygonal elements based on delaunay triangulation.

The first bracket on the left side of the equation is defined as the stiffness matrix  $K$ , the first term on the right side is the external force vector  $R_{ext}$ , and the second term represents the internal force vector  $R_{int}$ , then Eq. (35) can be abbreviated as:

$$K\Delta u_b = R_{ext} - R_{int} \quad (36)$$

After calculating the single stiffness, the elastic stiffness matrix of the whole domain can be obtained through the assembly according to degrees of freedom. Then the global equilibrium equation is offered as Eq. (37), in which  $\Delta u_b$  is the node displacement increment for the boundary of the whole domain.

$$(\sum K)\Delta u_b = \sum (R_{ext} - R_{int}) \quad (37)$$

Hammer quadrature is selected to solve the aforementioned equilibrium equation, and the integration scheme is shown in Fig. 3. Then the corresponding stiffness matrix and internal and external force vectors can be solved as follows.

$$K = \sum_{i=1}^{3n} [B_u^C]_i^T(\xi, s) D_e^i [B_u^C]_i(\xi, s) A_i \quad (38)$$

The external load vector  $R_{ext}$  can be extracted from Eq. (35) and is expressed as

$$R_{ext} = \int_{\Gamma} \Phi^T(\xi, s) f_t d\Gamma + \int_{\Omega} \Phi^T(\xi, s) f_b d\Omega \quad (39)$$

The first term on the right-hand-side of Eq. (39) is the distributed load on the boundary. It can be further simplified, considering that at the polyhedron boundary ( $\xi=1$ )  $\Phi(\xi, s)=N_u(s)$  applies. This can be written as

$$\int_{\Gamma} \Phi^T(\xi, s) f_t d\Gamma = \int_{-1}^1 N_u(s) |J(s)| f_t ds \quad (40)$$

The second term is the body load vector. For the case of a constant body load, this term is expressed by substituting Eq. (31) and integrating numerically with Gauss points as

$$\int_{\Omega} \Phi^T(\xi, s) f_b d\Omega = \sum_{k=1}^n \sum_{i=1}^3 [N_{ki}^u(s) \psi_u \xi_i^{-(0.5+S_n)} \psi_u^{-1}]^T f_b A_{ki} \quad (41)$$

where  $n$  represents the number of line elements in a polygon,  $k$  denotes the  $k^{\text{th}}$  triangle sector within a polygonal element and  $i$  denotes the  $i^{\text{th}}$  integration point in the triangular sector.

### 3. Numerical example verification

This section focuses on the rationality of the proposed method for numerical analysis. The stress concentration coefficient of the infinite plate with a circular hole is firstly calculated, and verified against theoretical solution. The stability is then discussed when the material is nearly incompressible. Subsequently, work examples on different opening shapes on structure are examined, in which flexibility and universality are testified.

#### 3.1. Circular hole in a square plate

Fig. 4(a) shows the geometry of a plate with a circular hole, and the schematic diagram for the solution is illustrated in Fig. 4(b). Theoretical solution derived from the classical continuum mechanics shows that the local stress disturbance caused by the opening mainly occurs in the range of 1.5 times the diameter of the hole [63]. To eliminate the influence generated from stress disturbance, the length  $l = 10r$  is selected for the square in this calculation example.

##### (1) Polygon mesh

In this paper, the polygon generation algorithm is mainly implemented in two steps: firstly, the background triangle mesh is automatically generated using CAE software; secondly, each vertex is taken as the center (marked with symbol  $\blacktriangle$ ), and the geometric center of all triangles sharing the center point are connected counterclockwise. A detailed sketch of the polygon elements generation process is provided in Fig. 5, and more information can be referred in literature [29,34].

##### (2) Quadtree mesh

Quadtree, commonly known as quadrant quadtree, is an efficient data structure in computer information science. The core principle is to



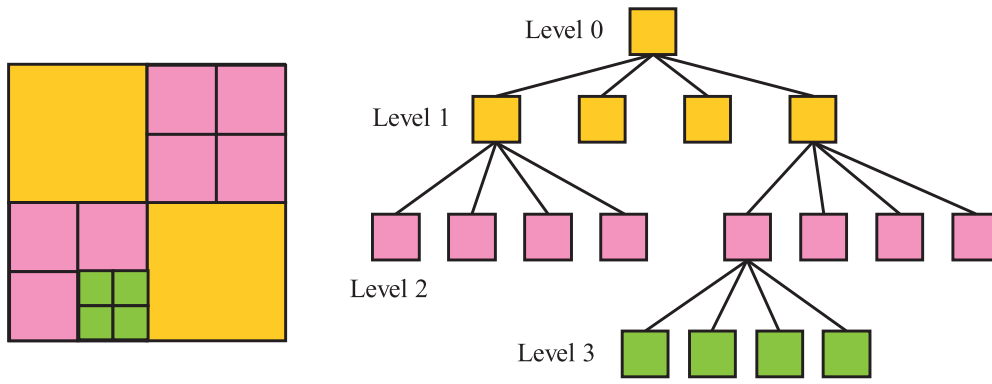


**Fig. 6.** An example of quadtree principle explanation.

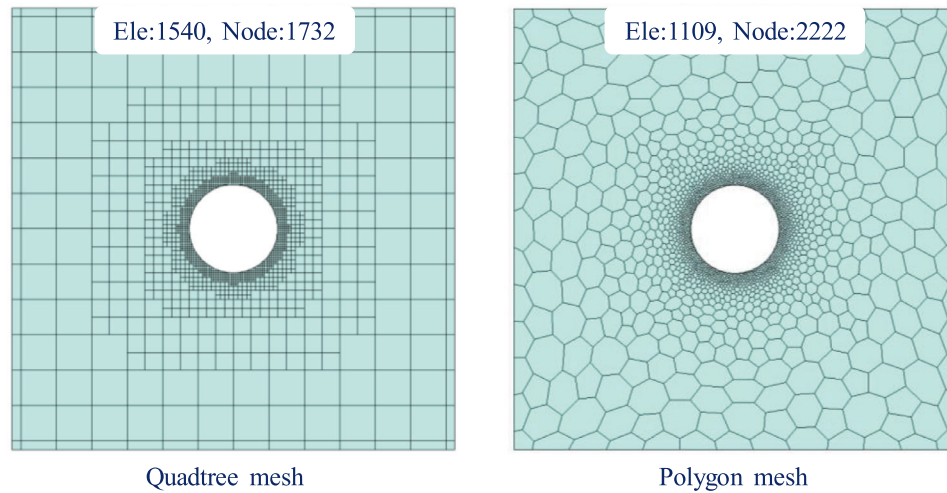
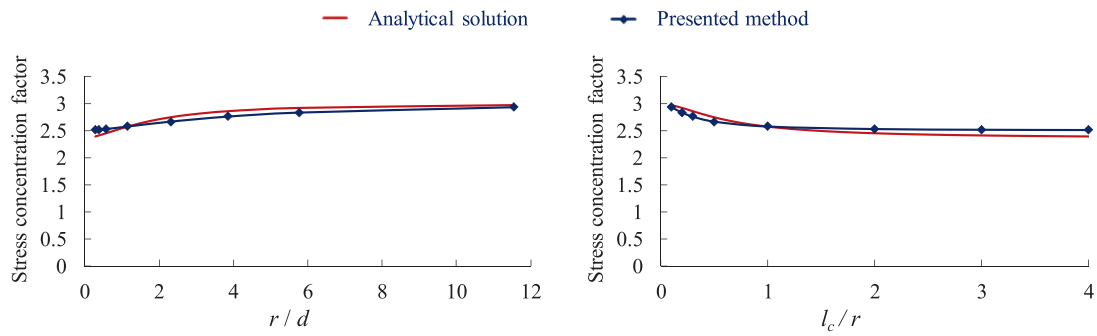
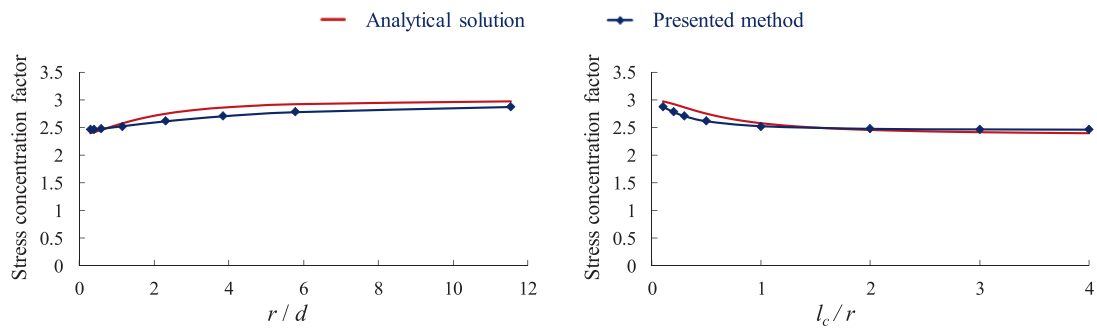


**Fig. 7.** Quadtree mesh and unstructured polygonal mesh.



(a) results of quadtree mesh



(b) results of polygon mesh

**Fig. 8.** Stress concentration factor with unstructured grid (Poisson's ratio  $\nu = 0.3$ ).

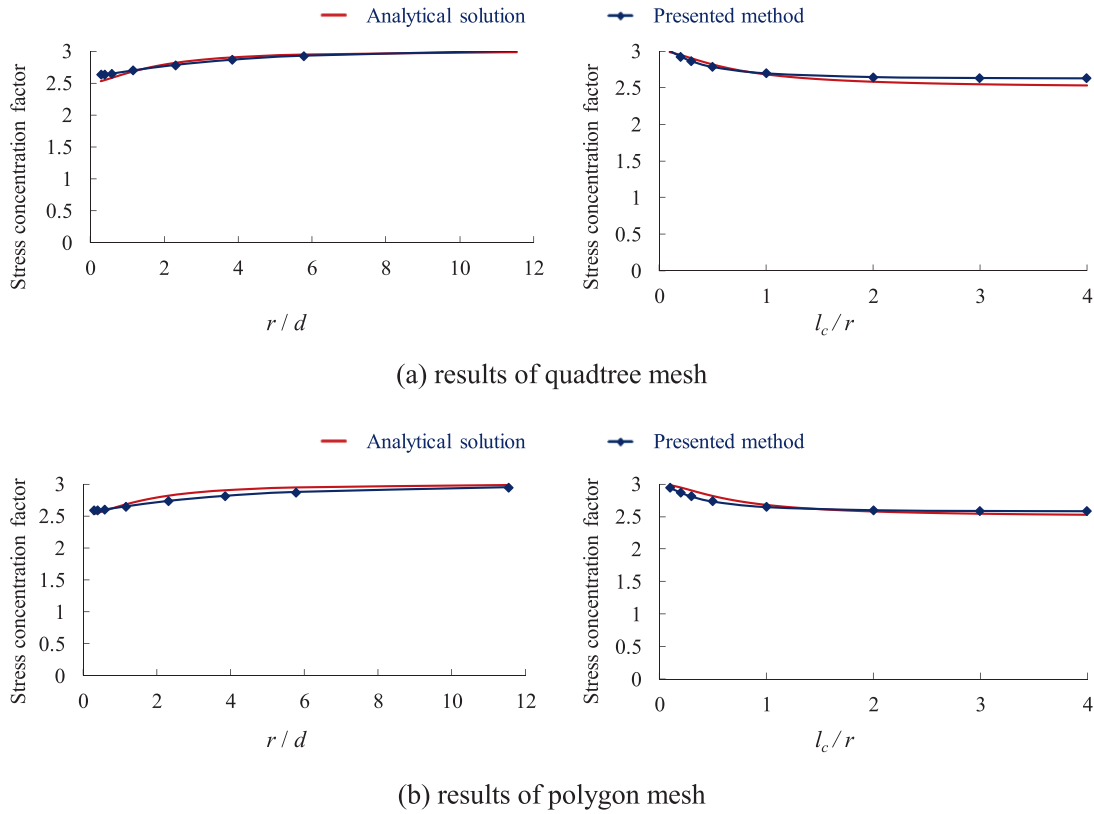


Fig. 9. Stress concentration factor with unstructured grid (Poisson's ratio  $\nu = 0.499$ ).

divide a square area into four quadrants regularly, and each quadrant is further divided into four sub quadrants, so that the sub quadrants are divided step by step until all the sub quadrants are uniform for the phenomenon represented (see Fig. 6 for an example of the principle). And detailed description and application simulations can be found in the literatures [32,35,46].

In this section, the aforementioned highly-efficient quadtree mesh and unstructured polygonal mesh generation technologies are introduced to discretize the calculation domain as shown in Fig. 7. As a results, 1540 elements with 1732 nodes, and 1109 elements with 2222 nodes are generated via quadtree and polygon scheme, respectively.

Base on experimental results, the stress concentration factor of the orifice is often smaller than that derived from the classical elastic theory due to the formulation of unique microstructure and inherent characteristic scale observed in the actual engineering materials [18]. The stress concentration factor can be reasonably weakened considering the internal length parameter of the material which shows better strain gradient of the orifice in SBFEM-Cosserat. Therefore, the stress concentration factor of the circular hole should be less than 3.0 using the Cosserat continuum [18],[19] (the classical continuum mechanical derivation value is 3.0 [63]).

In this calculation, modulus of elasticity  $E = 200$  GPa and Poisson's  $\nu = 0.3$  are selected, and the Cosserat shear modulus is set as follows:  $G_c/G = 0.5 = c$  and  $d = \frac{l_c}{2} \sqrt{\frac{1}{c} + 1}$ . Several internal length parameters are given in this discussion, including  $l_c = 0.1r, 0.2r, 0.3r, 0.5r, 1.0r, 2.0r, 4.0r, 8.0r$ , aiming to investigate the variation of the stress concentration factor at the hole edge in detail (the determination of parameters for Cosserat can be referred to literature [64]). The stress concentration factor is defined as the ratio of the tensile stress at the hole top to the uniform stress at the right boundary as shown in Fig. 8 where the proposed method mostly agreed with theoretical solution [18,19] with satisfactory accuracy in both quadtree and polygon mesh. With the vari-

Table 1

Comparisons of stress concentration factor obtained from different method.

Poisson's ratio	Method	Stress concentration factor (extremum)	
		Quadtree mesh	Polygon mesh
0.3	SBFEM classical continuum	3.33	3.25
	Proposed method	2.93	2.89
0.499	SBFEM classical continuum	3.51	3.48
	Proposed method	3.00	2.95

ation of the internal length parameter, the stress concentration coefficient tends to a certain value which is less than 3.0, indicating that the internal properties of materials can be reasonably considered using the proposed method. Through the aforementioned results, the correctness of the proposed method can be verified.

Besides, the stability of the proposed method is strengthened when considering this material as nearly incompressible (Poisson's ratio  $\nu = 0.499$ ) as shown in Fig. 9, wherein the incompressible materials can be simulated even more accurately.

In order to highlight the characteristics of the current proposed method, a comparisons to the classical continuum approach are included in Table 1. As it can be seen, due to the internal length parameter cannot be considered, the stress concentration factor obtained by the classical continuum method is higher than that from the proposed method, whichin the stress state at the hole edge might be overstated.

#### (1) Other holes in a square plate

The application to different hole forms is further verified by using the ellipse and diamond hole, as shown in Fig. 10(a). Among them, the long axis of an ellipse is  $a = r = 0.01$  m, the short axis is  $b = a/2$ . For

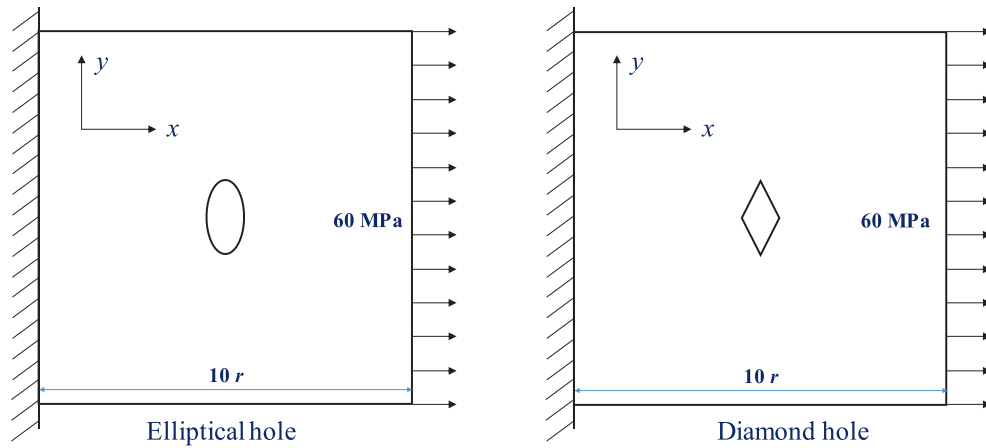
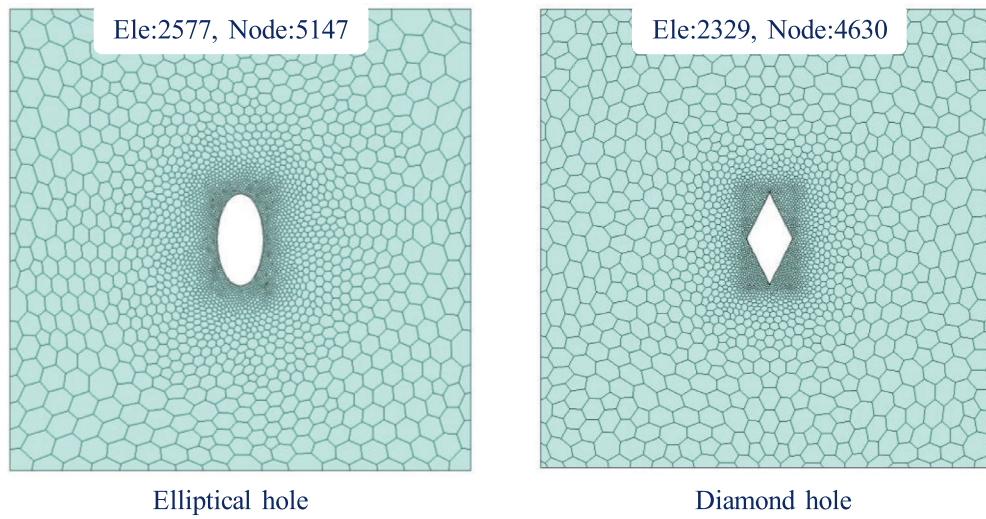


**Fig. 10.** Ellipse and diamond opening form and grid discretization.

(a) geometrical information



(b) polygon mesh

the rhombus, the long diagonal is set as 0.01 m, and the short diagonal takes half.

Polygon mesh discretization is exhibited in Fig. 10(b). The detailed parameters are defined as follows: elastic modulus  $E = 200$  GPa, Cosserat shear modulus  $G_c/G = 0.5$ , and internal characteristic length  $l_c = 0.001$  m.

The results of two kinds of opening forms under different Poisson's ratios are given in Fig. 11 and Fig. 12. The maximum stress occurs at the sharp top of hole edge, and good symmetry can be observed in the stress distribution, which conforms to the general rule. When Poisson's ratio is close to 0.5, the stress distribution remains normal, while the extreme value has increased. As a result, different opening structures can be simulated conveniently and reasonably using the proposed method, even for incompressible material.

The differences of stress extremum along  $x$  direction are listed in Table 2, as it can be seen, for elliptical hole, Cosserat continuum can weaken stress concentration from 3.34 GPa to 2.81 GPa (18.9%) relative to classical continuum theory. Similarly, this is reduced from 3.51 GPa to 3.05 GPa (15.1%) in terms of the Poisson's ratio is close to 0.5. And for rhombus hole, Cosserat continuum can weaken stress concentration from 9.64 GPa to 7.59 GPa (27.0%) relative to classical continuum theory. Similarly, this is reduced from 19.32 GPa to 14.85 GPa (30.1%) in terms of the Poisson's ratio is close to 0.5.

**Table 2**

Comparisons of stress concentration factor obtained from different method.

Poisson's ration	Method	Stress extremum along $x$ direction ( $\times 10^3$ MPa)	
		Elliptical hole	Rhombus hole
0.3	SBFEM classical continuum	3.34	9.64
	Cosserat continuum	2.81	7.59
Difference (%)		18.9	27.0
	0.499		
	SBFEM classical continuum	3.51	19.32
	Cosserat continuum	3.05	14.85
Difference (%)		15.1	30.1

#### 4. Application of complex opening structure

In this section, two examples are employed, containing complex open-hole structures, aiming to verify the flexibility, universality, and complex geometry adaptability of the proposed method.



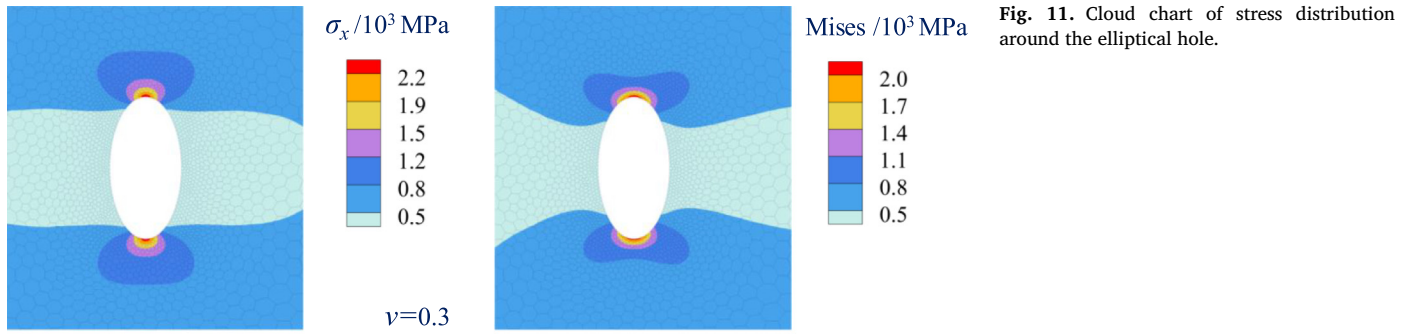
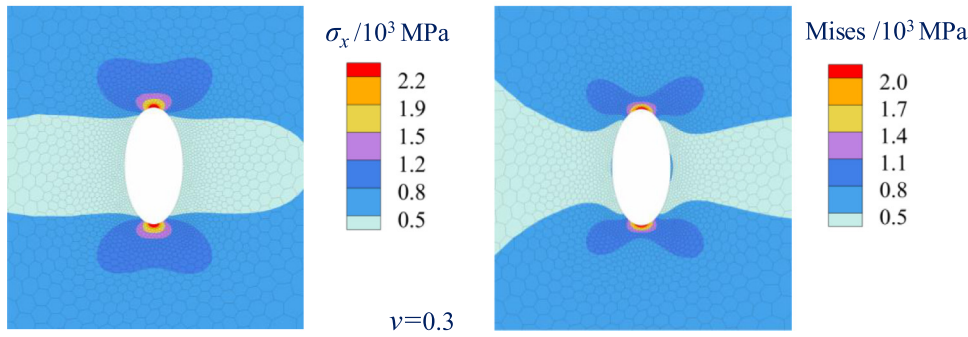
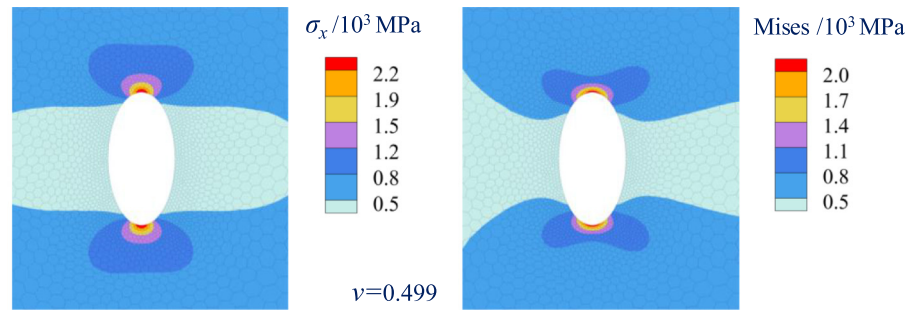


**Fig. 11.** Cloud chart of stress distribution around the elliptical hole.

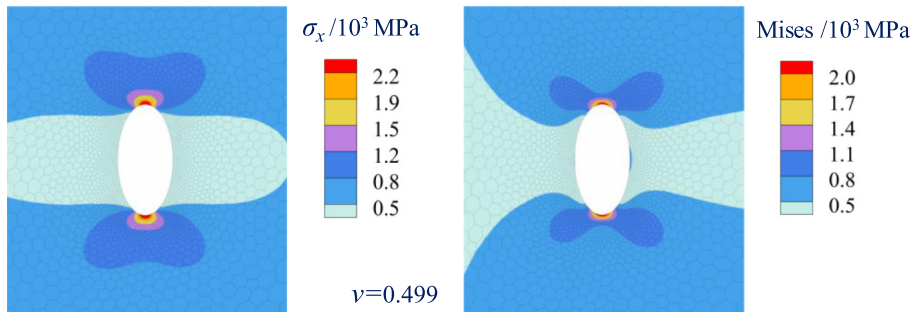
(a) Cosserat continuum



(b) SBFEM classical continuum



(c) Cosserat continuum



(d) SBFEM classical continuum

#### 4.1. Analysis of multiple circular hole structure

##### (1) Polygon mesh

The geometric information and polygon discretization of the first example is shown in Fig. 13. The side length of the plate is 0.5 m, and

the maximum diameter of the circular hole is 15.0 times the minimum diameter in this example. Polygonal generation technology is used to discretize the complex opening hole structure. The automatic discretization and the local refinement can be achieved around the circular hole after setting only the minimum and maximum mesh sizes. 5984 cells are generated with 11,965 nodes in this simulation.

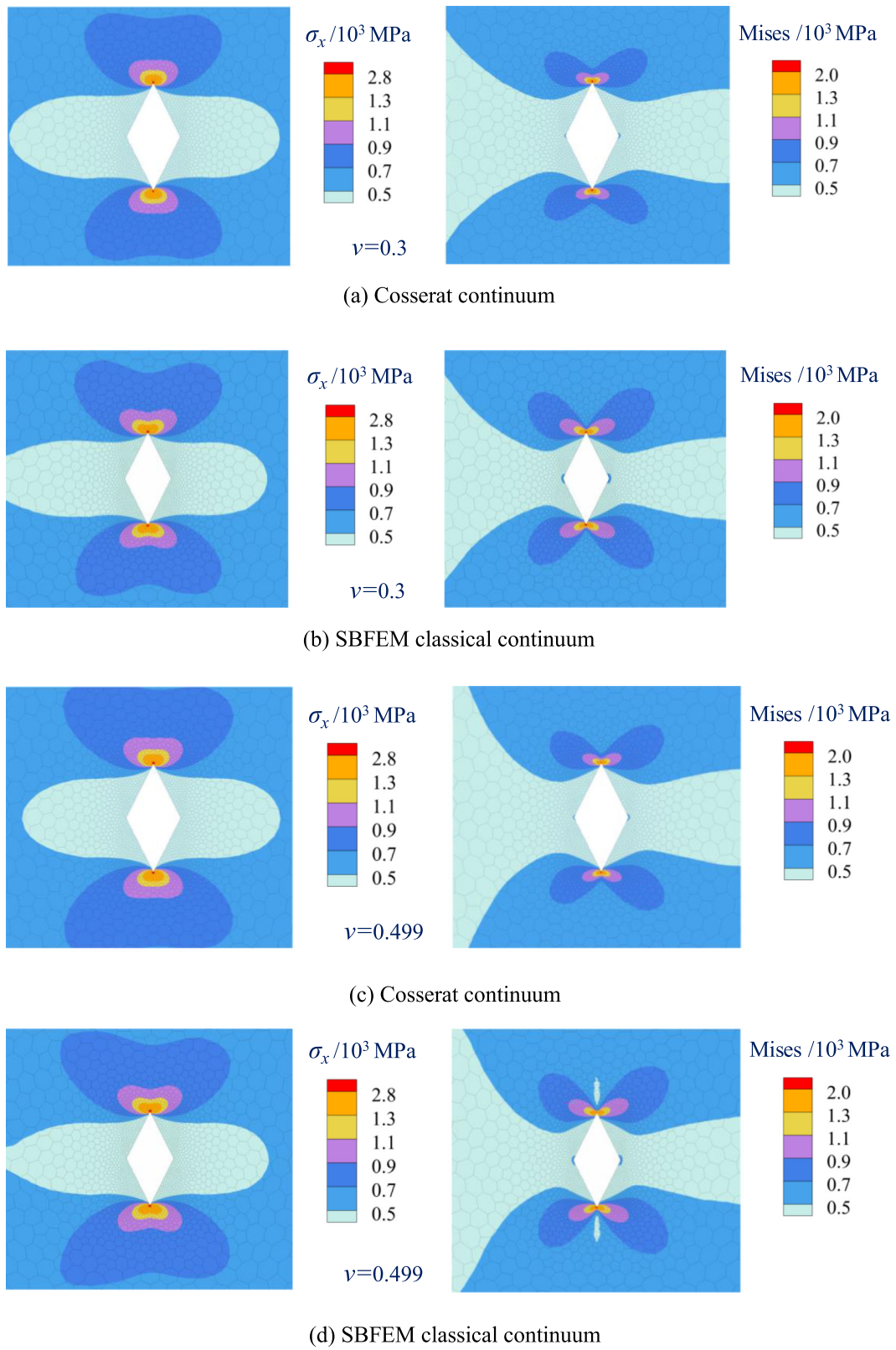


Fig. 12. Cloud chart of stress distribution around a rhombus hole.

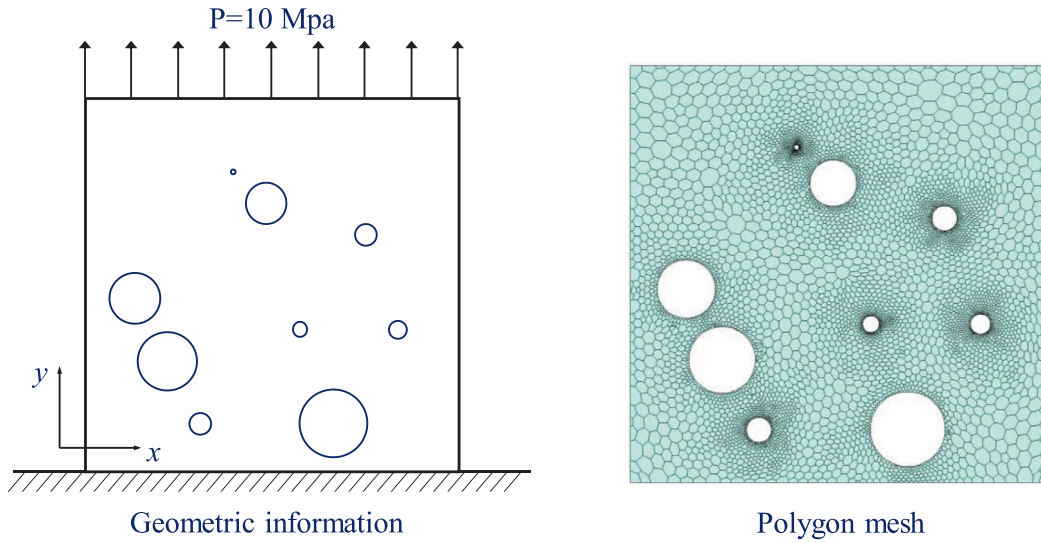


Fig. 13. Geometric and grid discretization of plate structures with multiple circular holes (polygon mesh).

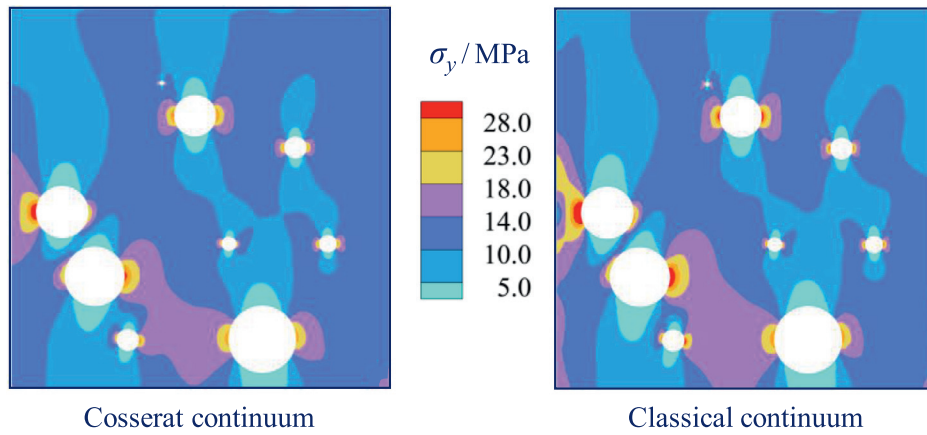
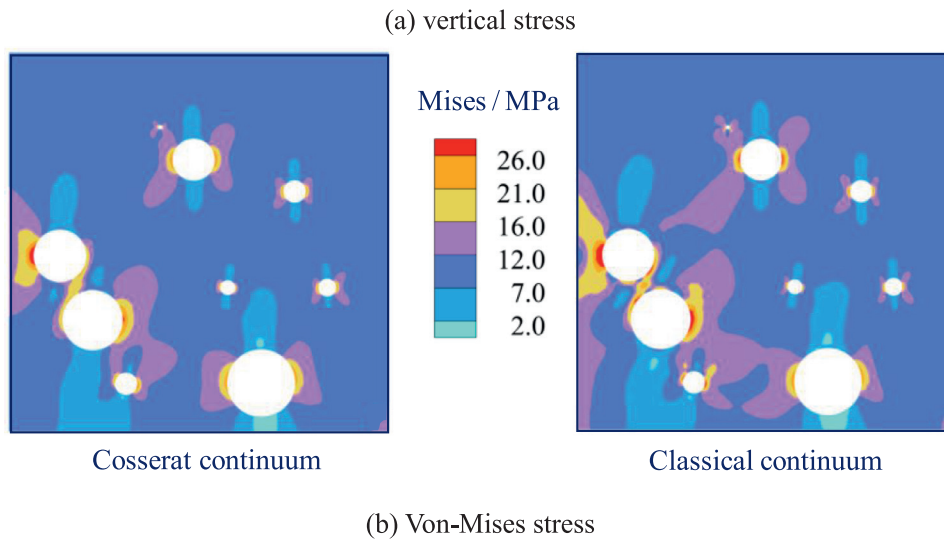
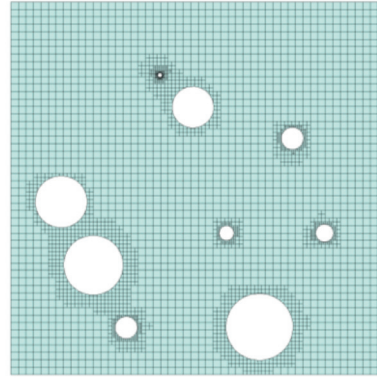
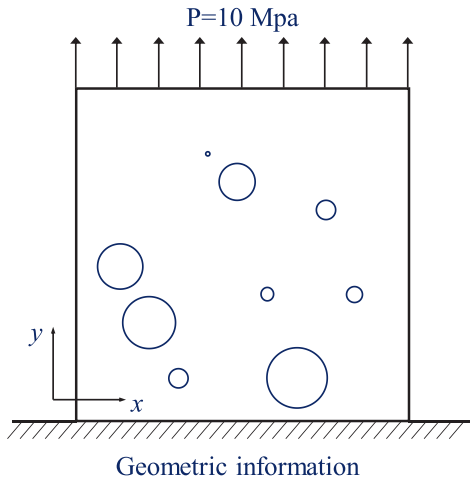


Fig. 14. Comparison results of plate structures with multiple circular holes.



The calculation is performed using SBFEM-Cosserat continuum and classical continuum theory, respectively. The calculation parameters are selected as follows: the bottom edge of the plate is constrained, a uniform load of 10.0 MPa is applied at the top, the elastic modulus  $E = 30.0$  GPa, and Poisson's ratio  $\nu = 0.2$ . Extra parameters for Cosserat is set as:  $G_c = 0.5$  G,  $l_c = 0.001$  m.

Analysis results in Fig. 14 show that the global distribution is generally the same of the two methods with differences in extreme values: from the perspective of vertical stress, SBFEM-Cosserat can weaken stress concentration from 43.0 MPa to 34.0 MPa (26.6%) relative to classical continuum theory. Similarly, this is reduced from 39.0 MPa to 31.0 MPa (25.8%) in terms of Von-Mises stress. The primary reason is



**Fig. 15.** Quadtree discretization of plate structures with multiple circular holes.

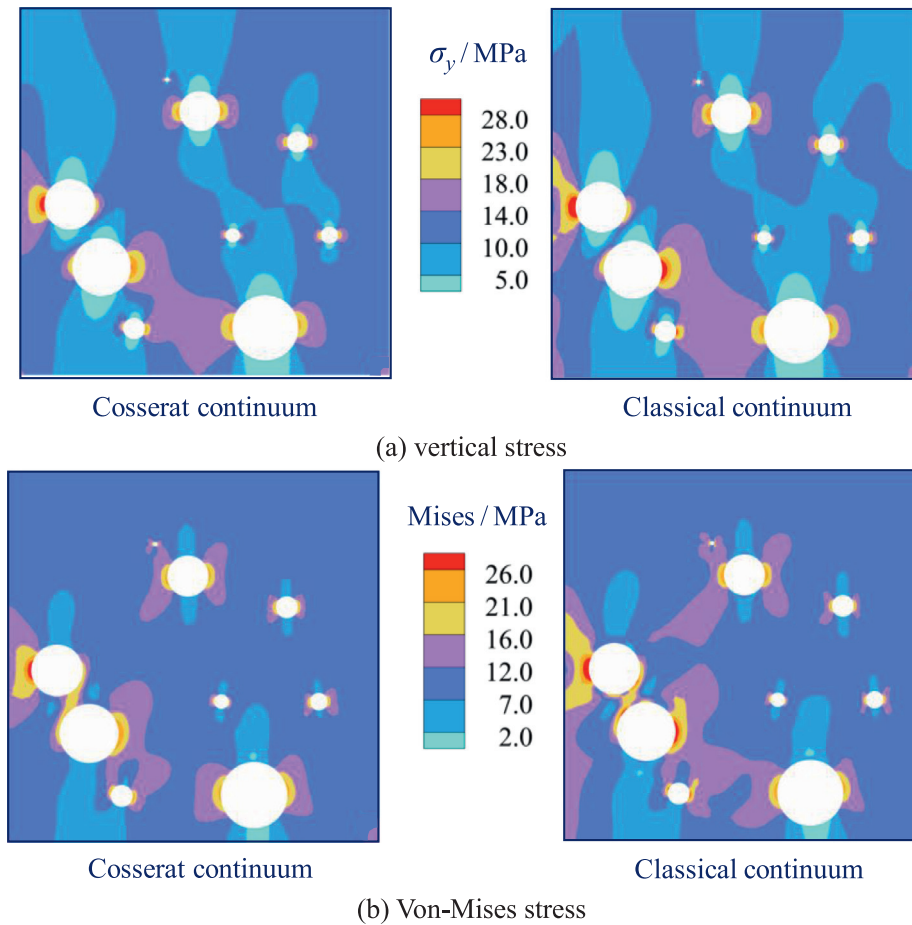


**Fig. 16.** Comparison results of plate structures with multiple circular holes (quadtree mesh).

that the element couple stress and the microstructure characteristics of materials can be considered in the former method.

## (2) Quadtree element

An efficient mesh subdivision algorithm is inherent in quadtree technology, enabling local mesh refinement can be achieved with less grids. And the technology has been utilized in the research work of relevant scholars [32,35,65]. Therefore, the simulation of multiple circular hole structure is recalculate using quadtree mesh. As it is shown in Fig. 15, a partial encryption scheme is adopted around the hole, as a result, a total of 3702 elements and 4132 nodes are generated.

The results are provided in Fig. 16, as it can be seen, the stress distributions are consistent with aforementioned polygon grids. In general, the stress concentration at the hole edge can be weakened using the presented SBFEM-Cosserat method, indicating the quadtree technology can be introduced to further enhance the performance of managing complex geometries.

## (3) Quadrilateral element

As stress gradient around the hole edge changes greatly, a refined mesh is necessary to accurately replicate the stress state around the hole. However, it is inconvenient to achieve scale variation efficiently with



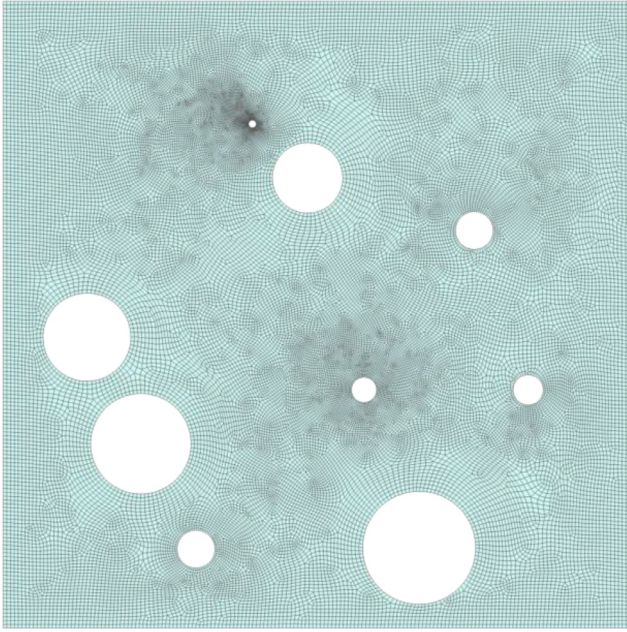


Fig. 17. Quadrilateral element with automatic discretization.

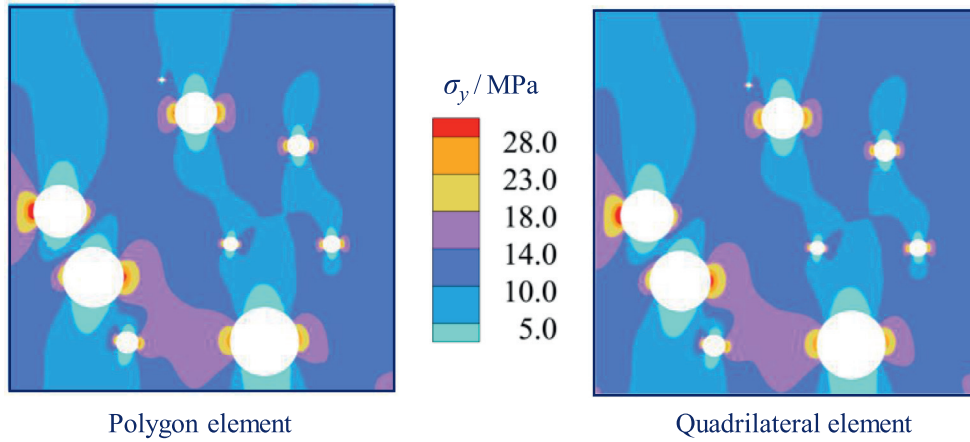
the shape restriction of the classical quadrilateral element. Thus, more grids have to be generated (36,456 elements with 37,061 nodes in total) in Fig. 17.

The presented SBFEM-Cosserat continuum and the same parameters are utilized in this simulation. Results of different grids are provided in Fig. 18. The distributions of the classical quadrilateral element are consistent with those of the polygon element. Therefore, the computation efforts can be reduced through the variation of element size.

## 5. Conclusion

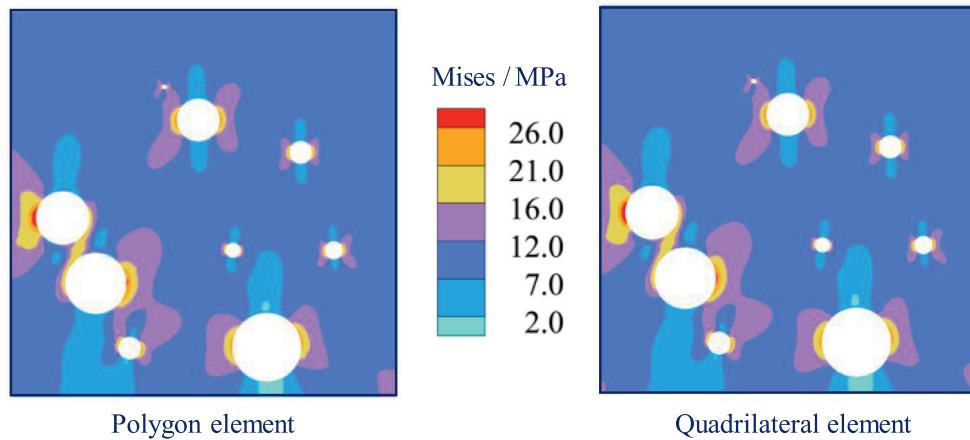
In this paper, a newly SBFEM-Cosserat polygonal element is proposed via formulating and programming the theory of the Cosserat continuum under the SBFEM framework. The stress concentration induced by different opening forms on thin plate structures are investigated, and the rationality and applicability of the presented method are also discussed. The main conclusions can be summarized as follows:

- (1) The generality and flexibility of the Cosserat continuum have been enhanced. The proposed method has access to solving arbitrary polygon mesh over quadrilateral FEM which has limitations on the element shape. Benefit by this, the efficient quadtree and polygon discretization technology can be combined seamlessly so that the analysis performance of the Cosserat continuum is improved when disposing complex geometries and opening hole structures.



(a) vertical stress

Fig. 18. Comparison of distribution using different grids.



(b) Von-Mises stress



- (2) The stability of the Cosserat continuum has been further improved. The results are in good agreement with the theoretical solution, indicating that the presented method is credible and reasonable for numerical analysis. More importantly, the results remain to be identical with the analytical solution, even when the material is nearly incompressible. Enabling the limitation to be circumvented, namely, the volume self-locking would be emerged, resulting in a loss of precision, when the Poisson's ratio approximates to 0.5 using the conventional method.
- (3) The stress concentration can be reasonably weakened considering the internal length parameter of the material which shows better strain gradient of the orifice in SBFEM-Cosserat, making the stress state of the structure would be described more reasonably. For the simulation of square plate with multiple circular holes, the differences of two methods in extreme values are provided: from the perspective of vertical stress, SBFEM-Cosserat can weaken stress concentration from 43.0 MPa to 34.0 MPa (26.6%) relative to classical continuum theory. Similarly, this is reduced from 39.0 MPa to 31.0 MPa (25.8%) in terms of Von-Mises stress.

This method could be employed to improve the efficiency of design, analysis, and optimization of complex opening structures, which is the focus of our future research. Furthermore, more advantages will emerge when extending the method to three-dimension and strain localization analysis.

#### Declaration of Competing Interest

None.

#### Acknowledgements

This work was supported by the National Natural Science Foundation of China (Grant Nos. U1965206, 51890915, 52009018) and the China Postdoctoral Science Foundation (Grant Nos. BX20190056, 2020M670752).

#### Reference

- [1] Seifi M, Salem A, Satko D, et al. Defect distribution and microstructure heterogeneity effects on fracture resistance and fatigue behavior of EBM Ti-6Al-4V[J]. *Int J Fatigue* 2017;94(pt.2):263–87.
- [2] Muskhelishvili N I. Some basic problems of the mathematical theory of elasticity[M]. Springer Science & Business Media; 2013.
- [3] Kirsch G. Die theorie der elastizitat und die bediirfnisse der festigkeitslehre[M], 42. Springer; 1898. p. 797–807.
- [4] Green AE. General bi-harmonic analysis for a plate containing circular holes[J]. *Proceed R Soc Lond. Ser A. Math Phys Sci* 1940;176(964):121–39.
- [5] Ling CB. On the stresses in a plate containing two circular holes[J]. *J Appl Phys* 1948;19(1):77–82.
- [6] Meguid SA, Shen CL. On the elastic fields of interacting defense and main hole systems[J]. *Int J Mech Sci* 1992;34(1):17–29.
- [7] Meguid SA, Gong SX. Stress concentration around interacting circular holes: a comparison between theory and experiments[J]. *Eng Fract Mech* 1993;44(2):247–56.
- [8] Ting K, Chen KT, Yang WS. Stress analysis of the multiple circular holes with the rhombic array using alternating method[J]. *Int J Press Vessels Pip* 1999;76(8):503–14.
- [9] Ting K, Chen KT, Yang WS. Boundary element alternating method applied to analyze the stress concentration problems of multiple elliptical holes in an infinite domain[J]. *Nucl Eng Des* 1999;187(3):303–13.
- [10] Thomas SB, Mhaskar MJ, Sethuraman R. Stress intensity factors for circular hole and inclusion using finite element alternating method[J]. *Theor Appl Fract Mech* 2000;33(2):73–81.
- [11] Chou SI. Stress field around holes in antiplane shear using complex variable boundary element method[J]. *J Appl Mech* 1997;64(2):432–5.
- [12] Wang YB, Chau KT. A new boundary element for plane elastic problems involving cracks and holes[J]. *Int J Fract* 1997;87(1):1–20.
- [13] De Borst R. Simulation of strain localization: a reappraisal of the Cosserat continuum[J]. *Eng Comput (Swansea)* 1991;8(4):317–32.
- [14] Li X, Tang H. A consistent return mapping algorithm for pressure-dependent elasto-plastic Cosserat continua and modelling of strain localization [J]. *Comput Struct* 2005;83(1):1–10.
- [15] Tang H, Sun F, Zhang Y, et al. Elasto-plastic axisymmetric Cosserat continua and modelling of strain localization[J]. *Comput Geotech* 2018;101:159–67.
- [16] Tang H, Wei W, Liu F, et al. Elasto-plastic Cosserat continuum model considering strength anisotropy and its application to the analysis of slope stability[J]. *Comput Geotech* 2020;117:103235.
- [17] Tordesillas A, Peters JF, Gardiner BS. Shear band evolution and accumulated microstructural development in Cosserat media[J]. *Int J Numer Anal Methods Geomech* 2004;28(10):981–1010.
- [18] Mindlin RD. Influence of couple-stresses on stress concentrations[R]. Columbia University New York; 1962.
- [19] Liu J, Huang M, Ge XR. Solution of Stress Concentration Problem Considering Influence of Couple-Stress[J]. *J Shanghai Jiaotong Univ (Chin Ed)* 2001;35(10):1481–5.
- [20] Zhao Y, Zhang RJ. Finite element analysis of stress concentration problem based on cosserat theory [J]. *Chin Quart Mech* 2009;30(3):410–14.
- [21] Providas E, Kattis MA. Finite element method in plane Cosserat elasticity[J]. *Comput Struct* 2002;80(27–30):2059–69.
- [22] Zhang H, Wang H, Liu G. Quadrilateral isoparametric finite elements for plane elastic Cosserat bodies[J]. *Acta Mech Sin* 2005;21(4):388–94.
- [23] Tang HX, Guan YH, Zhang X, et al. Low-order mixed finite element analysis of progressive failure in pressure-dependent materials within the framework of the Cosserat continua. *Eng Comput (Swansea)* 2017;34(2):251–71.
- [24] Khoei AR, Yadegari S, Biabanaki SOR. 3D finite element modeling of shear band localization via the micro-polar Cosserat continuum theory[J]. *Comput Mater Sci* 2010;49(4):720–33.
- [25] Godio M, Stefanou I, Sab K, et al. Dynamic finite element formulation for Cosserat elastic plates[J]. *Int J Numer Methods Eng* 2015;101(13):992–1018.
- [26] Alsaleh M. Numerical modeling of strain localization in granular materials using cosserat theory enhanced with microfabric properties[J]; 2004.
- [27] Tang H, Dong Y, Wang T, et al. Simulation of strain localization with discrete element-Cosserat continuum finite element two scale method for granular materials[J]. *J Mech Phys Solids* 2019;122:450–71.
- [28] Milbradt P, Pick T. Polytope finite elements[J]. *Int J Numer Methods Eng* 2008;73(12):1811–35.
- [29] Sukumar N, Tabarraei A. Conforming polygon finite elements[J]. *Int J Numer Methods Eng* 2004;61:2045–66.
- [30] Sukumar N. Quadratic maximum-entropy serendipity shape functions for arbitrary planar polygons[J]. *Comput Methods Appl Mech Eng* 2013;263(263):27–41.
- [31] Chen K, Zou D, Kong X, et al. A novel nonlinear solution for the polygon scaled boundary finite element method and its application to geotechnical structures[J]. *Comput Geotech* 2017;82:201–10.
- [32] Song CM. *The Scaled Boundary Finit Element Method[m]*. Hoboken: John Wiley & Sons Ltd; 2018.
- [33] Liu J, Lin G. A scaled boundary finite element method applied to electrostatic problems[J]. *Eng Anal Bound Elem* 2012;36(12):1721–32.
- [34] Ooi ET, Shi MG, Song CM, et al. Dynamic crack propagation simulation with scaled boundary polygon elements and automatic remeshing technique[J]. *Eng Fract Mech* 2013;106:1–21.
- [35] Ooi ET, Natarajan S, Song C, et al. Dynamic fracture simulations using the scaled boundary finite element method on hybrid polygon quadtree meshes[J]. *Int J Impact Eng* 2016;90:154–64.
- [36] Huang YJ, Yang ZJ, Liu GH, et al. An efficient FE-SBFE coupled method for mesoscale cohesive fracture modelling of concrete[J]. *Comput Mech* 2016;58(4):635–55.
- [37] Jiang SY, Du CB, Ooi ET. Modelling strong and weak discontinuities with the scaled boundary finite element method through enrichment[J]. *Eng Fract Mech* 2019;222:106734.
- [38] Zhang P, Du CB, Carolin B, et al. A scaled boundary finite element method for modelling wing crack propagation problems[J]. *Eng Fract Mech* 2019;216:106466.
- [39] Li YT, Zhong H, Pang L, et al. Influence of the water pressure distribution along crack faces on seismic fracture modeling of a dam-reservoir-foundation system[J]. *Eng Anal Bound Elem* 2019;101(Apr):252–69.
- [40] Huynh HD, Zhuang X, Nguyen-Xuan H. A polytree-based adaptive scheme for modeling linear fracture mechanics using a coupled XFEM-SBFEM approach[J]. *Eng Anal Bound Elem* 2020;115(Jun):72–85.
- [41] Chen D, Birk C, Song C, et al. A high-order approach for modelling transient wave propagation problems using the scaled boundary finite element method[J]. *Int J Numer Methods Eng* 2014;97(13):937–59.
- [42] Birk C, Behnke R. A modified scaled boundary finite element method for three-dimensional dynamic soil-structure interaction in layered soil[J]. *Int J Numer Methods Eng* 2012;89(3):371–402.
- [43] Li P, Liu J, Lin G, et al. A NURBS-based scaled boundary finite element method for the analysis of heat conduction problems with heat fluxes and temperatures on side-faces[J]. *Int J Heat Mass Transf* 2017;113:764–79.
- [44] Xu H, Zou D, Kong X, et al. Study on the effects of hydrodynamic pressure on the dynamic stresses in slabs of high CFRD based on the scaled boundary finite-element method[J]. *Soil Dyn Earthquake Eng* 2016;88:223–36.
- [45] Liu J, Lin G, Li J. Short-crested waves interaction with a concentric cylindrical structure with double-layered perforated walls[J]. *Ocean Eng* 2012;40:76–90.
- [46] Saputra A, Talebi H, Tran D, et al. Automatic image-based stress analysis by the scaled boundary finite element method[J]. *Int J Numer Methods Eng* 2017;109(5):697–738.
- [47] Zou D, Chen K, Kong X, et al. An enhanced octree polyhedral scaled boundary finite element method and its applications in structure analysis[J]. *Eng Anal Bound Elem* 2017;84:87–107.
- [48] Chen K, Zou D, Kong X. A nonlinear approach for the three-dimensional polyhedron scaled boundary finite element method and its verification using Koyna gravity dam[J]. *Soil Dyn Earthquake Eng* 2017;96:1–12.

- [49] Chen K, Zou D, Kong X, et al. Global concurrent cross-scale nonlinear analysis approach of complex CFRD systems considering dynamic impervious panel-rock-fill material-foundation interactions[J]. *Soil Dyn Earthquake Eng* 2018;114:51–68.
- [50] Chen K, Zou D, Kong X, et al. An efficient nonlinear octree SBFEM and its application to complicated geotechnical structures[J]. *Comput Geotech* 2018;96:226–45.
- [51] Liu J, Zhang PC, Lin G, et al. High order solutions for the magneto-electro-elastic plate with non-uniform materials[J]. *Int J Mech Sci* 2016;115:532–51.
- [52] Liu J, Hao CK, Ye WB, et al. Free vibration and transient dynamic response of functionally graded sandwich plates with power-law nonhomogeneity by the scaled boundary finite element method. *Comput Methods Appl Mech Eng* 2021;376:113665.
- [53] Ye WB, Liu J, Zang QS, et al. Buckling analysis of three-dimensional functionally graded sandwich plates using two-dimensional scaled boundary finite element method[J]. *Mech Adv Mater Struct* 2021(3):1–16.
- [54] Zhang ZH, Liu Y, Dissanayake DD, et al. Nonlocal damage modelling by the scaled boundary finite element method[J]. *Eng Anal Bound Elem* 2018;99(Feb):29–45.
- [55] Zhang ZH, Dissanayake DD, Saputra AA, et al. Three-dimensional damage analysis by the scaled boundary finite element method[J]. *Comput Struct* 2018;206(Aug):1–17.
- [56] Gong J, Zou D, Kong X, et al. A coupled meshless-SBFEM-FEM approach in simulating soil-structure interaction with cross-scale model[J]. *Soil Dyn Earthquake Eng* 2020;136:106214.
- [57] Zou D, Sui Y, Chen K. Plastic damage analysis of pile foundation of nuclear power plants under beyond-design basis earthquake excitation[J]. *Soil Dyn Earthquake Eng* 2020;136:106179.
- [58] Qu Y, Zou D, Kong X, et al. Seismic cracking evolution for anti-seepage face slabs in concrete faced rockfill dams based on cohesive zone model in explicit SBFEM-FEM frame[J]. *Soil Dyn Earthquake Eng* 2020;133(Jun.) 106106.1-106106.14.
- [59] Liu Y, Saputra Albert A, Wang JC, et al. Automatic polyhedral mesh generation and scaled boundary finite element analysis of STL models[J]. *Comput Methods Appl Mech Eng* 2017;313:106–32.
- [60] Gravenkamp H, Duczek S. Automatic image-based analyses using a coupled quadtree-SBFEM/SCM approach[J]. *Comput Mech* 2017;60:559–84.
- [61] He Y, Guo J, Yang H. Image-based numerical prediction for effective thermal conductivity of heterogeneous materials: a quadtree based scaled boundary finite element method[J]. *Int J Heat Mass Transf* 2019;128(JAN):335–43.
- [62] Liu L, Zhang J, Song C, et al. Automatic scaled boundary finite element method for three-dimensional elastoplastic analysis[J]. *Int J Mech Sci* 2020;171:105374.
- [63] Xu ZL. A concise course in elasticity[M]. Beijing: Higher Education Press; 2002. p. 8.
- [64] Tang H X, Li X K. Numerical analysis for the effects of constitutive parameters in Cosserat continuum model on the simulation results of the strain localization[J]. *Chin J Mech Eng* 2008;25:676–81.
- [65] Chen X, Luo T, Ooi ET, et al. A quadtree-polygon-based scaled boundary finite element method for crack propagation modeling in functionally graded materials[J]. *Theor Appl Fract Mech* 2018;94:120–33.